A search for life in Palaeoproterozoic marine sediments using Zn isotopes and geochemistry

A. El Albani [a,*], K.O. Konhauser [b], A. Somogyi [c], J. Ngwalghoubou Ikouanga [a], A. Lamboux [d], J. Blichert-Toft [d,e], E. Chi-Fru [f], C. Fontaine [a], A. Mazurier [a], A. Riboulleau [g], A.-C. Pierson-Wickmann [h], F. Albarède [d,e]

[a] *Institut de Chimie des Milieux et Matériaux, Université de Poitiers and CNRS, 86073 Poitiers, France*
[b] *Department of Earth and Atmospheric Sciences, University of Alberta, Edmonton, AB T6G 2E3, Canada*
[c] *Nanoscopium Beamline Synchrotron Soleil, BP 48, Saint-Aubin, Gif-sur-Yvette 91192, France*
[d] *Laboratoire de Géologie de Lyon, CNRS UMR 5276, Ecole Normale Supérieure de Lyon, and Université de Lyon, 69007, Lyon, France*
[e] *Department of Earth, Environmental and Planetary Sciences, Rice University, Houston, TX 77005, USA*
[f] *School of Earth and Ocean Sciences, Centre for Geobiology and Geochemistry, Cardiff University, Cardiff LF10 3AT, Wales, UK*
[g] *UMR 8187 CNRS LOG, University of Lille, ULCO, Villeneuve d'Ascq 59655, France*
[h] *Geosciences Rennes, CNRS UMR 6118, Université de Rennes, Rennes Cedex, 35042, France*

ARTICLE INFO

ABSTRACT

Sediments from the 2.1- to 1.9-billion-year-old Francevillian Group in southeastern Gabon include centimeter-sized pyritized structures suggestive of colonial organisms (El Albani et al., 2010), some of which may have been motile (El Albani et al., 2019). However, these interpretations were largely based on morphological and geochemical characteristics that lack metabolic clues and/or can be explained by abiotic processes. To move this work forward, we describe other centimeter-sized specimens, loosely referred to as lenticular forms (LF), from the same area and apply a more holistic approach including morphology, mineralogy, and geochemistry. The objects are 0.2–4 cm in diameter, and most of them are endowed with a regular brim that scales proportionally to external diameter reminiscent of biological order, hence rendering the LF putative biogenic traces. The LF are perfectly delineated in every direction and deflect the sedimentary layers on which they rest. X-ray microtomography further demonstrates that the LF are syn-depositional features and not concretions, while lead isotope systematics indicate that the geochemical imprint of diagenesis is inconsequential. Low sulfur content is largely concentrated in the organic matrix, and scarcity of pyrite and its persistence as micron-sized crystals show that the role of sulfate reduction is minor. Most interestingly, the fillings of the LF cavities show large and correlated excesses of organic carbon and zinc, with the latter being distinctly enriched in its light isotopes. The geochemical anomalies of the fillings relative to the host rock, notably those associated with Zn, clearly were buried with the LF, and further imply biogenicity. In this regard, a ten-fold increase in LF size towards the top of the black shale series hosting the LF might be related to increasing Zn (nutrient) availability. Although we cannot conclude with any certainty what these remnant organisms were, their features all taken together are evocative of very large agglutinate protists that grazed on bacterial biomass either in the water column or as benthic mats.

© 2023 Elsevier B.V. All rights reserved.

1. Introduction

The composition of the Archean and Palaeoproterozoic biosphere remains uncertain largely due to the scarcity of an unequivocal Precambrian palaeobiological record. The recovery of benthic microfossils – the physical remains of microorganisms that grew attached to ancient sediments – has provided relevant guidance for understanding the trajectory of biological evolution (Butterfield, 2007; Knoll, 2014), but ultimately their interpretation is based primarily on subjective morphological features. The difficulties associated with such determinations are well-identified and repeatedly reviewed (see a recent account with references in Neveu et al., 2018). In short, abiotic processes can almost always explain features reminiscent of microfossils. Moreover, demonstrating the bio-

logical nature of putative fossil remains in ancient terrestrial rocks is a formidable challenge due to post-depositional alteration via burial, lithification, and secondary fluid flow through porous and fractured rocks (Neveu et al., 2018).

Spectroscopy and geochemistry offer another approach. Vibrational, infrared, and Raman spectroscopy, for example, allows the molecular compounds present in organic material and the thermal maturity of a fossil to be determined (Hickman-Lewis et al., 2016; Olcott Marshall and Marshall, 2015). Carbon isotope analysis (Rosing, 1999; Tashiro et al., 2017) of carbonaceous remains adds a strong component to help determine the biogenic character, or not, of a given relic. But both techniques are sensitive to metamorphic alteration and to date have been more efficient at characterizing unambiguous fossils and less at providing incontrovertible proof of the nature of enigmatic biological traces (Marshall et al., 2005; Sforna et al., 2014), particularly in carbon-rich materials. Trace elemental geochemistry as a tool suitable for the quest of biogenicity has also been applied. Using microbeam particle-induced X-ray emission (μPIXE), Hickman-Lewis et al. (2020) demonstrated association of transition metals and metalloids with carbonaceous materials in 3.33 Ga-old cherts from the Barberton greenstone belt and suggested that patterns in elemental abundance might help constrain the metabolic networks present in fossilized ecosystems. Gangidine et al. (2021) analyzed hot-spring deposits from the mid-Paleozoic Drummond Basin, Australia, but the elements for which they identified excesses associated with putative fossils would normally qualify as terrigenous for modern oceanographers. Sforna et al. (2022) recently showed associations of nickel with putative porphyrins in Proterozoic microfossils. Sedimentological evidence for a biological role of this highly toxic and poorly chelated element in organic-rich material still remains ambiguous as nickel isotope analysis suggests that isotope fractionation may be an effect of the weathering environment (Porter et al., 2014). Other micronutrients, notably cobalt, copper, iron, manganese, and molybdenum are all essential for biological activity, yet most of these elements are redox-sensitive and, thus, their concentrations and isotopic signatures, whenever more than one isotope is present, are readily overprinted by the decay of organic matter and diagenesis (Wacey, 2009).

Apart from iron, zinc is the most abundant trace element in modern plankton (Twining and Baines, 2013) and, therefore, is particularly useful as a potentially strong biosignature. Further, Zn^{2+} is non-toxic, redox-*insensitive*, and of all the transition elements, it shows the highest affinity for a large spectrum of ligands of biological interest. This makes Zn a versatile element in thousands of proteins of biological interest, in particular as a co-factor of carbonic anhydrase, alkaline phosphatase, zinc fingers, and other biological components (Weber et al., 2018). Zinc is known to be protective against oxidative and saline stress as well as increasing membrane stability in plants (Tufail et al., 2018). Importantly, unlike carbon and nitrogen, Zn has the potential for preserving both chemical and isotopic memories of biological precursors of cyanobacteria, algae, and other aquatic photoautotrophs. Preferential uptake of light Zn isotopes by organic material has been shown clearly by earlier Zn isotope work on modern carbonates (Pichat et al., 2003) and on the water column (Weber et al., 2018), but has not so far been explicitly considered as a useful biogenicity indicator. This is the purpose of the present work, which makes a strong case in favor of Zn abundances and isotopic compositions as a new biosignature.

Contrary to complex and potentially misleading morphological criteria, with well-known cases being the ALH84001 Martian meteorite (Neveu et al., 2018), 'cyanobacterial filaments' in the 3465 Ma Apex Chert in the Pilbara Craton, Western Australia (Brasier et al., 2002), and the purported stromatolites from the 3.7 Ga old Isua supracrustal belt, southwest Greenland (Allwood et al., 2018),

well-resolved spectroscopic and geochemical measurements are repeatable by any observer or analyst with a reproducible outcome. Here we focus primarily on the geochemical approach and test whether, among other geochemical tracers, Zn and its isotopes may help track ancient life on early Earth and other planets.

Specifically we address the issue of biogenicity in deep-time sedimentary rocks by using a particular group of putative biological traces found in sediments from the Francevillian series deposited in the 2.1 to 1.9 Gy interval, previously described in a series of publications (El Albani et al., 2010, 2014, 2019) and referred to here as lenticular forms (LF). The decisive advantages of the Gabon putative life forms over those from the Late Proterozoic and the Cambrian, such as the Burgess Shale (Butterfield et al., 2007; Gaines et al., 2019; Powell, 2003), is their very mild degree of diagenesis, their huge enrichment in organic carbon (up to 10%) and bitumen, and their deposition in an oxygen-poor, clay-rich environment that offers a higher degree of preservation potential. We combine macroscopic and tomographic morphological evidence with a broad coverage of major and trace element and isotopic evidence, with emphasis on Zn, to address hotly debated questions that generally accompany ancient putative traces of life:

a) Could biological-like morphology be an artefact of early or late diagenesis or even be concretions?
b) What is the chemical imprint of diagenesis and in particular the role of sulfate reduction?
c) If the enigmatic investigated traces are of biogenic origin, which order do they represent, typically prokaryotes vs eukaryotes, multicellular colonial vs metazoan organisms?

In addition to the issue of biogenicity, the present work is relevant to two other broad questions pertinent to early life reconstruction. First, could the emergence of eukaryotes, largely believed to have taken place at the onset of the Mesoproterozoic ~1.6 Gy ago, instead have arisen much earlier (Javaux and Lepot, 2018; Knoll, 2014)? Second, what is the relevance of the putative Gabon life forms to the ~2.1 Ga old Lomagundi event, a period characterized by the burial of organic matter and increased atmospheric oxygenation (Melezhik et al., 2013; Canfield et al., 2013; Mänd et al., 2020).

2. Geological and sedimentary setting

The Francevillian basin consists of 35,000 km^2 of unmetamorphosed sedimentary rocks that were deposited on the margin of the Birimian (Eburnean) craton during the Palaeoproterozoic Eon in an epicontinental setting in what is now the Republic of Gabon, western equatorial Africa (Bonhomme et al., 1982; Bros et al., 1992; Reynaud et al., 2018) (Fig. 1). The sediment package is between 1000 and 2500 m thick and is subdivided into four lithostratigraphic units, FA to FD, which rest unconformably on Archean basement rocks. The FA unit mainly consists of fluviatile and deltaic sandstones. At the top, it contains uranium enrichments and hosts the well-known Oklo natural nuclear reactors (Gauthier-Lafaye et al., 1989). These reactors are heat sources that trigger the convection of interstitial fluids. The FB unit consists of marine sediments deposited mainly below the storm wave base. It has been recognized as the source of massive petroleum generation which played a major role in the formation of the uranium-rich deposits that generated the Oklo natural nuclear reactors (Mossman, 2001). Because of its diverse lithological composition, the FB unit is further divided into the FB1 (a, b, and c) and FB2 (a and b) subunits. The FB1a and FB1b subunits consist of interlayered shales, sandstones, and conglomerates, fining upwards to predominantly shales at the top. The FB1c subunit consists of shales, but also contains a thin iron formation overlain by
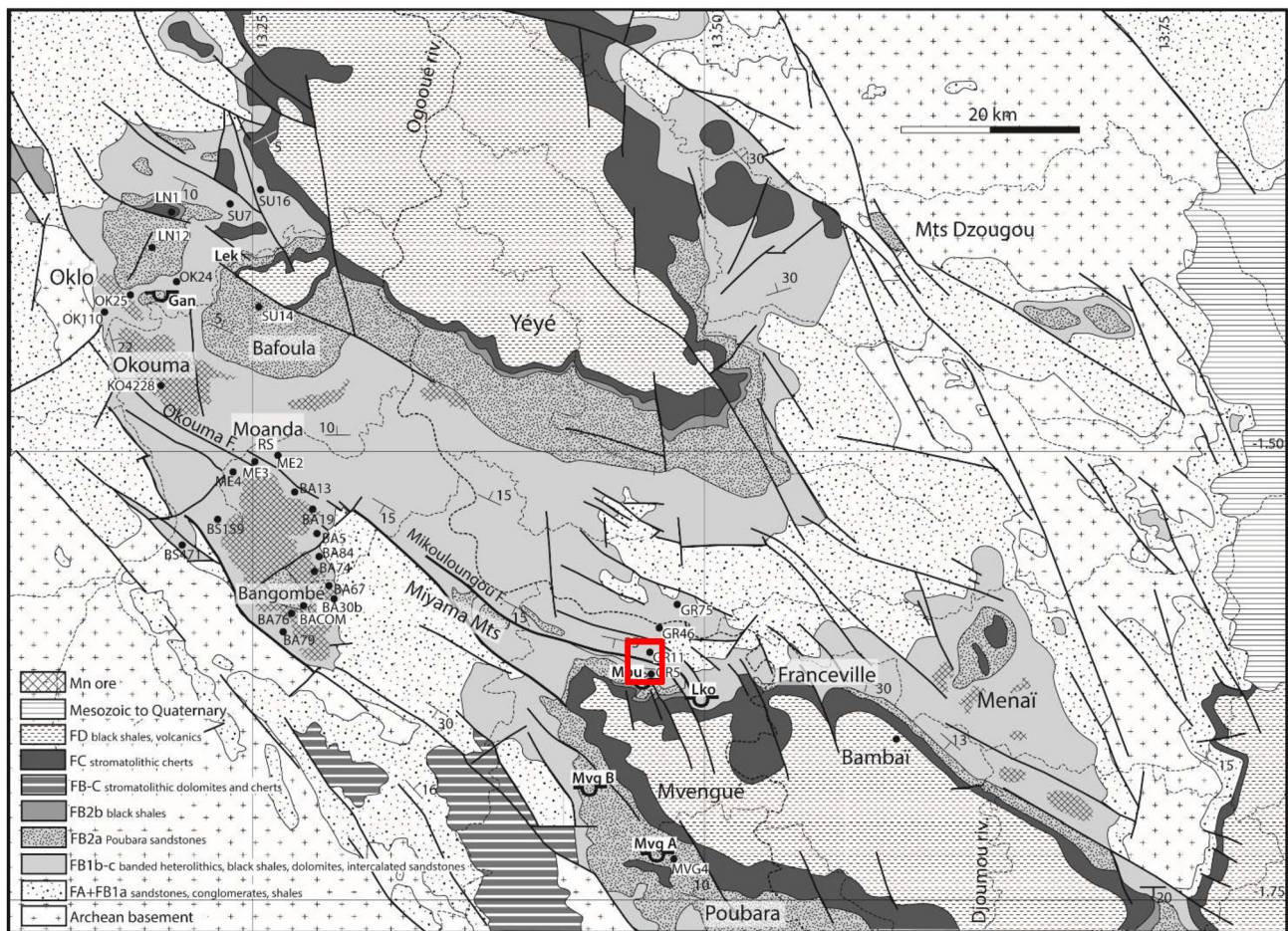
Fig. 1. Geological map of the Franceville Basin. The studied outcrops are located in the Moulende quarry (red square). Structural framework and unit contours modified from Weber (1968) and Gauthier-Lafaye (1986).

black shales and a thick interval rich in manganese. The FB2a sub-unit consists of sandstone beds deposited in channels near the fair-weather wave base. These are sharply overlain by the FB2b subunit including finely-laminated black shales (Fig. 2) interbedded with thin siltstone layers deposited by waning storm surges. All of the specimens presented here were collected from the FB2b black shales (Fig. 2). In the quarry that was investigated, the FB2b black shales are 5 m thick. The overlying FC unit is dominated by dolomites and stromatolitic cherts, indicating shallow-water conditions. The FD unit corresponds to black shales deposited during a transgressive phase. A large portion of the Francevillian series was deposited during the Lomagundi-Jatuli Event carbon isotope excursion dated in the Transfennoscandian Greenstone Belt at ca. 2.22–2.06 Ga (Canfield et al., 2013; Martin et al., 2013) but, on a global scale, it may be basin-specific or diachronous and could locally extend to younger ages (Martin et al., 2015). The preservation of randomly ordered smectite-rich illite/smectite mixed layer minerals (R0-type) demonstrates unusually slow mineral transformation and only a moderate degree of diagenesis, which is remarkable considering the Palaeoproterozoic age of the sedimentary succession (Gauthier-Lafaye et al., 1996). It also has no indication of hydrothermal influence (Gauthier-Lafaye et al., 1996).

Previous publications assessed that the Francevillian black shales were deposited from an oxygenated water column in a quiet, low-energy marine environment (Canfield et al., 2013; El Albani et al., 2010). They are interbedded with thin sandstone layers lacking specimens. They are distributed without significant overlap on the black-shale bedding planes. Fine laminae, prevailing in the enclosing shales, surround the LF specimens investigated here with

a selection illustrated in Fig. 3 and Fig. S1. This indicates that the structures were in place before burial compaction as illustrated in Fig. 4. Most specimens are filled with fine-grained sediments, yet some are only represented as impressions. Both molds and impressions are commonly preserved in three dimensions.

3. Materials and methods

About 300 LF specimens with exquisitely preserved morphologies were collected from the FB2b subunit at the Moulendé Quarry within a ~5 m thick black-shale layer dominated by silts and clays (El Albani et al., 2010, 2019). They were photographed at the University of Poitiers using a Nikon Europe D610 digital single-lens reflex camera equipped with a Nikon AF-S 24–120 mm f/4G ED VR lens. The textural contrasts between a given LF specimen's filling and its host rock were investigated on polished slab sections with a ZEISS Discovery V8 stereoscope coupled with an Axio Cam ERc 5s microscope camera.

Described as one of the largest Palaeoproterozoic accumulations of organic matter in the world and based on their high total organic carbon (TOC) at current high maturity (Mossman, 2001), the FB black shales are widely regarded as the source rocks of the remarkably large oil field of Franceville. Liquid hydrocarbon, the remnants of which have since solidified, was generated through the "oil window" ($<100\,°C$) (Mossman et al., 2005). Such low temperatures make Raman geothermometers unsuitable to assess the intensity of metamorphism. Beyssac et al.'s (2002, 2003) thermometer is best calibrated above $300\,°C$, while the peak-width thermometer of Kouketsu et al. (2014) is unreliable below $150\,°C$

Fig. 2. (Top) View of the outcop: the 5 m-thick finely horizontally laminated black shales are interbedded with thin, silty sandstone layers hosting the LF (black arrow), which are homogeneously distributed throughout the section. **(Bottom)** The white arrow shows the body of an LF specimen, while the yellow arrow points to its brim.

and has an uncertainty of $\pm50\,°C$. In addition, the Raman spectra of organic carbon depends not only on the maximum temperature but also on the nature of the organic precursor (Quirico et al., 2009). In particular, Phanerozoic organic material cannot be used as reference for establishing temperatures on early sediments. Raman spectra were therefore not obtained.

3.1. Synchrotron radiation induced X-ray fluorescence (SR-XRF) analysis

Polished slab sections of representative samples were chosen for scanning X-ray fluorescence analysis. The SR-XRF measurements were performed on several areas within the studied samples at the Nanoscopium hard X-ray nanoprobe beamline (Somogyi et al., 2015) at Synchrotron Soleil, France. The monochromatic X-ray beam of 18 keV energy was focused on the sample area by a Kirckpatrick-Baez nano-focusing mirror. Micrometer resolution for elemental maps of mm^2–sized sample areas was obtained by implementing the fast continuous scanning (FLYSCAN) technique. Full XRF spectra were collected for each pixel of the scans by two Si-drift detectors (VITUS H50, KETEK GmbH) in order to increase the solid angle of detection. The XRF sum-spectra of the measured regions were fitted by the PyMCA software (Solé et al., 2007) to identify the elements detectable in the samples. The spatial distribution of the identified elements, S, K, Ca, Ba, Mn, Fe, Ni, Cu, Zn, Ga, Ge, As, Se, Pb, Sr, and Zr, was reconstructed by an in-house Matlab code, which also corrects for spectral overlapping. Each elemental intensity map was then corrected for the variation of the incoming X-ray intensity and measurement dead-time and was normalized to 10 ms/pixel exposure time. The semi-quantification of the elemental distribution maps was obtained by a home-made Matlab code converting the measured intensity distributions into mass fractions by using calibration factors obtained by measuring a known sample in the same measurement conditions.

3.2. X-ray microtomography

Micro-computed tomography (microtomography or micro-CT) analyses were done at the University of Poitiers on an RX-solutions EasyTom XL Duo equipment, which has one micro- and one nanofocus (LaB6 filament) Hamamatsu X-ray source coupled to a Varian PaxScan 2520DX flat panel. Reconstructions were done with the XAct software (RX-solutions) using a classical filtered back projection algorithm and reduction of beam hardening artefact. Virtual sections, 3D rendering, and videos were done with Avizo Fire v.9.2 (FEI).

3.3. X-ray diffraction

Approximately the same quantity of whole-rock powder and clay mineral fraction ($<2\,\mu m$) from 28 samples (14 LF fillings and 14 samples of their host rock) were analyzed with a Bruker D8 ADVANCE diffractometer at the University of Poitiers using $CuK\alpha$ radiation operating at 40 kV and 40 mA. The $<2\,\mu m$ clay fraction was separated by dispersion of gently hand-crushed bulk samples in deionized water with an Elma S60 ultrasonic agitation device without any chemical pre-treatment. The dispersed particles were allowed to settle under gravity at a controlled room temperature of $20\,°C$ and centrifuged to separate the $<2\,\mu m$ clay fraction. Oriented slides were prepared by drying ~1 mL of suspension on glass slides at room temperature. Analysis of whole-rock powder samples was performed over an angular range of $2–65°$ 2θ with a step size of $0.025°$ 2θ per 3 s. Oriented slides of the $<2\,\mu m$ clay fraction were analyzed at a step size of $0.02°$ 2θ per 3 s counting time and over 2 to $30°$ 2θ angular range after successive air drying (AD) and ethylene glycol (EG) saturation. Oriented samples were then prepared and analyzed in AD and EG states. Background stripping, indexing of peaks, and mineral identification were done using Bruker Eva software by comparing with International Centre for Diffraction Data (ICDD) files. The results were compared with reference data. We fitted one experimental sample from each lithology (LF fillings and host rock) in AD and EG states. Instrumental and experimental factors, such as the divergence slit, goniometer radius, soller slits, sample length, and quartz reference intensity, which are specific to the Bruker D8 ADVANCE diffractometer, were introduced. Sigmastar and the mass adsorption coefficient for Cu radiation were set to 13 and 45 $cm^2\,g^{-1}$, respectively.

3.4. Electron microscopy

Samples were carbon coated and imaged with an FEI Quanta 200 scanning electron microscope (SEM) equipped with an energy-dispersive X-ray spectrometer (EDX) at the Universities of Poitiers and Lille. Mineral identification and documentation of textural relationships were acquired in back-scattered electron mode (BSE) operated at an accelerating voltage of 15 kV, 1 nA beam current, and a working distance of 10.5 mm.
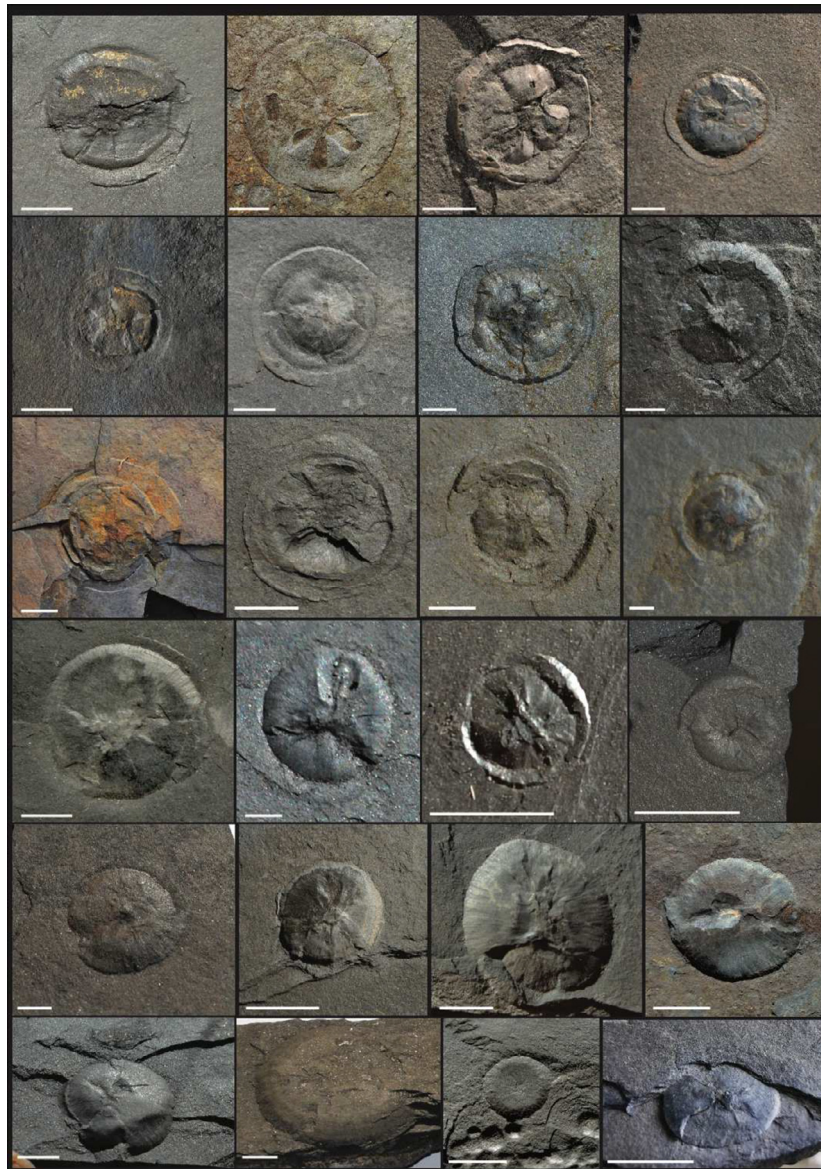
Fig. 3. Plate of 24 photographs of lenticular forms (LF) embedded in their black shale host rock (from subunit FB2b) arranged in a (row × column) array. Scale bars represent 1 cm. The morphology is lenticular, occasionally segmented by radial structures (e.g., 1 × 2, 1 × 3, 3 × 1, 4 × 1), and the outline is circular. A brim is present in some of the specimens (e.g., 1 × 1, 1 × 2, 1 × 4, 2 × 2, 3 × 2). Other samples miss the brim (e.g., 5×3, 5 × 4, 6 × 1, 6 × 3). This dichotomy may represent a contrast between the bottom and the top of the organism or be a preservation artefact. The dome part is filled with organic-rich clay.

3.5. Whole-rock chemical analysis

Major, trace, and rare-earth element abundances were determined on 14 LF fillings (specimens) and 14 host rock samples (the host sediments) at Service d'Analyse des Roches et Minéraux (SARM) of the Centre de Recherches Pétrographiques et Géochimiques (CRPG), Nancy, France, following the technique described by Carignan et al. (2001).

3.6. Carbon abundance and $\delta^{13}C$ analysis

Fourteen LF fillings and 14 host rock samples were powdered for the measurement of organic matter content. A FlashEA 1112 (ThermoFisher Scientific) CHNS analyzer was used for flash dynamic combustion at 970 °C under a constant helium flow. The Eager 300 software was used for data acquisition. A calibration curve was performed with aspartic acid and nicotinamide before each analysis. The measured carbon content includes both inorganic and organic carbon, but whole-rock geochemical data show that CaO contents are low. The analytical technique used for Thietal2019$\delta^{13}C$ analysis was described by Mercuzot et al. (2021). The data are listed in the Supplementary material.

3.7. Zinc and lead isotope analysis

Lead and Zn were separated by anion-exchange column chromatography and their isotopic compositions measured by multiple-collector inductively coupled plasma mass spectrometry (MC-ICP-MS) at the Ecole Normale Supérieure de Lyon (ENS Lyon). Ultrapure water and distilled nitric acid (HNO_3), hydrochloric acid (HCl), and hydrobromic acid (HBr) were used throughout.

About 100 mg of bulk sample was digested in a Savillex PFA beaker using 3 mL concentrated HCl and 0.5 mL concentrated HNO_3 at 100 °C for 72 h. After evaporation to dryness, 2 mL concentrated HCl were added for a second round of digestion at 100 °C for 24 h. The digested sample was evaporated to dryness and redissolved in 0.2 mL 2M HBr at 100 °C for 2 h, evaporated to dryness, and redissolved in 1 mL 2M HBr for chromatographic separation
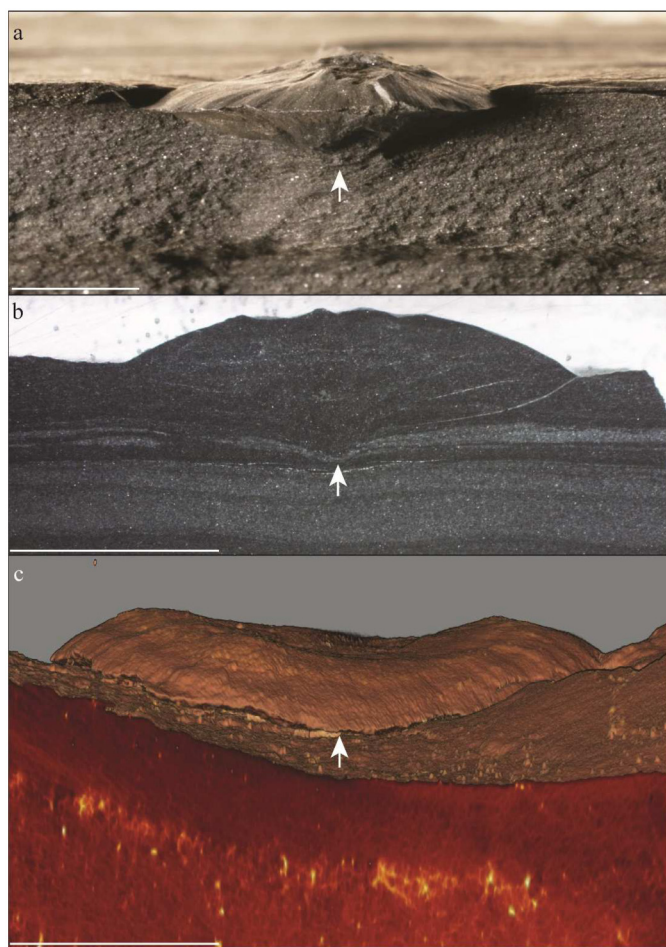
Fig. 4. (a) Biconvex LF specimen surrounded by its host rock. White arrows in all panels show the upper and lower apex, respectively. Scale bars in all panels are 1 cm. (b,c) Two cross-sections showing the relationship between an LF specimen and its underlying sediment. (b) Reflected-light microscopic view. (c) Three-dimensional color X-ray microtomography. In both cases, the LF is clearly observed to deflect the underlying laminae (white arrows), which attests that the LF are syn-depositional features and not secondary concretions.

of Pb and Zn on micro-columns filled with 0.5 mL new Biorad AG1-X8 (100–200 mesh) resin. Samples were centrifuged prior to loading the supernatant onto the anion-exchange columns, which had been cleaned with 6M HCl and preconditioned with 2M HBr. The sample matrix was discarded with 3 mL 2M HBr, while Pb was eluted with 3 mL 6M HCl and Zn was eluted with 3 mL 0.5M HNO_3. Zinc was purified a second time following the same elution protocol. The procedural blanks were <300 pg (Pb) and <30 ng (Zn).

The Pb isotope compositions were analyzed on a Nu Plasma 500 HR MC-ICP-MS at ENS Lyon using a DSN100 desolvation nebulizer system. Samples were dissolved in distilled 0.05M HNO_3 with 5 ppb Tl and concentrations were adjusted to 30 ppb. Instrumental mass bias was corrected using Tl while the accuracy of the measurements was adjusted by sample-standard bracketing relative to NIST SRM 981 (the Pb isotopic Standard Reference Material (SRM) 981 from the National Institute of Standards and Technology (NIST)) (Albarède et al., 2004). NIST 981 was measured systematically every second sample throughout each individual run session allowing for a final normalization to the double-spike values of Eisele et al. (2003). The repeated measurements of NIST SRM 981 yielded an external reproducibility <100 ppm (0.01%) for ^{204}Pb-normalized ratios and <50 ppm (0.005%) for $^{207}Pb/^{206}Pb$ and $^{208}Pb/^{206}Pb$. Zinc isotope abundances also were analyzed on
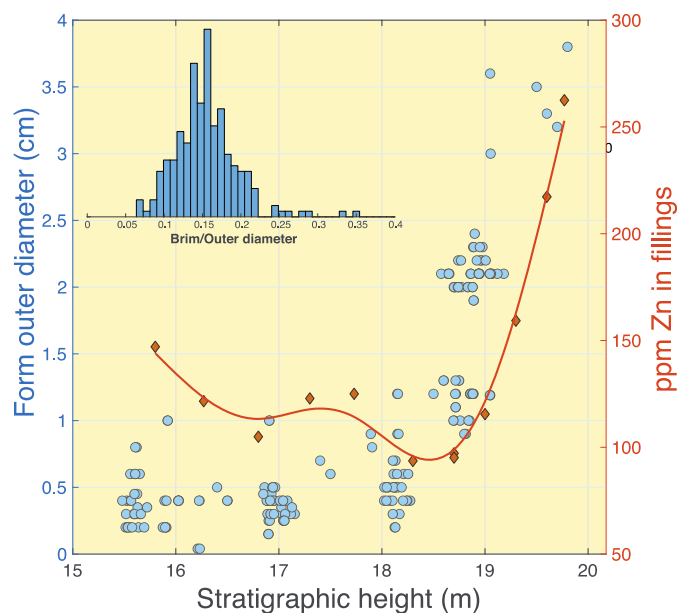

Fig. 5. Lenticular form diameters (in blue) and Zn contents of their fillings (in red) vs stratigraphic height. Jitter has been applied to the x-axis for better readability. The red curve is a fit of the filling data with a smoothing spline. The sharp increase of both parameters starting at 18.5 m indicates that a sudden increase in nutrient supply contributed to the ten-fold increase in organism size. Inset: Histogram of the brim/external diameter ratio, which shows that the geometric characteristics of the LF remain in constant proportion, a feature indicative of a biological origin.

the Nu Plasma 500 HR MC-ICP-MS at ENS Lyon but without desolvation. Instrumental mass bias was corrected using Cu NIST SRM 976 and sample-standard bracketing (Albarède et al., 2004). Zinc concentrations were adjusted to 200 ppb by dilution with 0.05M HNO_3. The Zn isotopic compositions are reported in parts per 1000 relative to the Lyon JMC in-house standard in delta notation. Typical $\delta^{66}Zn$ error bars are 0.05‰. The Pb and Zn isotope data are listed in the Supplementary material.

4. Results

4.1. Sample morphology

Visual observation (Figs. 3 and 4) and X-ray tomography reveal lenticular to circular shapes with radial symmetry (Fig. S1). Many specimens are rimmed by a mm-wide brim (Fig. 2 and Fig. 3), with a width proportional to the object size. The significance of samples with and without brims is unclear. Some specimens presented in Fig. 3 and Fig. S1 further show a radial pattern. Whether this pattern signals the presence of internal compartments in some individuals or a particular mechanical behavior of the LF will be discussed in a separate paper. Back-scattered electron and microtomography images of cross-sections demonstrate that the LF deflect the underlying sedimentary laminae (Fig. 4). Their diameters vary systematically with stratigraphic height (Fig. 5), ranging from 0.2 to 1 cm at the bottom of the black-shale layer and continue to increase systematically to >3 cm (almost 4 cm) at the top of the succession.

4.2. Grain size and mineralogy

Based on scanning electron microscopy-back-scattered electron imaging (SEM-BSE) coupled to energy-dispersive X-ray spectrometry (EDX), the LF show a stark contrast with it host sediments (Fig. 6). The LF have a fine-grained composition, with a sharp contact with the host sediments. The composition of the LF is typically enriched in clay minerals and organic carbon. Metal sulfides and

Fig. 6. Scanning electron microscopy-back-scattered electron imaging (SEM-BSE) coupled to energy-dispersive X-ray spectrometry (EDX) showing contrast in textural and mineralogical compositions within the LF comparing to the host rock. The yellow line traces the contact between the LF specimen and its host rock. It shows very clearly to the naked eye that the grain size of quartz, micas, and chlorite are coarser and more randomly distributed in the host rock than in the LF specimen. White scale bar is 1 mm.

Table 1
Mineralogical and geochemical contrasts between host rock and LF fillings. Parameter p measures the probability that the LF and their host rock belong to the same population (t-test). The standard asterisk scale is *** for $p < 0.001$, ** for $p < 0.01$, and * for $p < 0.05$.

Host rock	LF fillings	p
40% clay minerals	70% clay minerals	n/a
av. diameter of quartz grains 50 μm	av. diameter of quartz grains 25 μm	n/a
$C = 0.16 \pm 0.05$ mol/100 g	$C = 0.22 \pm 0.06$ mol/100 g	*
High Si, K, Zr, Hf	High Na, Ca, Er-Lu	***
High CAI	High Na/K, Lu/Hf	
av. [Zn] $= 94 \pm 40$ ppm	av. [Zn] $= 175 \pm 54$ ppm	***
av. δ^{66}Zn $= 0.36 \pm 0.10‰$	av. δ^{66}Zn $= 0.10 \pm 0.10‰$	***
av. ^{206}Pb/^{204}Pb $= 16.70 \pm 0.25$	av. ^{206}Pb/^{204}Pb $= 17.14 \pm 0.33$	**

carbonate minerals are absent. The clay minerals are parallel to the bedding and aligned along the perimeter of the specimens. This relationship confirms pre-compactional formation of the LF, resulting in local rearrangement of sediment grains during compaction. In this regard, taphonomical preservation occurred during early burial by the decay of organic matter leading to the complexation of organic matter with hydrous fine-sized clay minerals uniformly filling the available space provided by the LF.

The bulk X-ray mineralogical data on both the fillings and the host black shales show the presence of quartz, micas, illite, chlorite, and other clay minerals (Fig. 6 and Fig. S2). The grain-size of the LF is clearly finer than that of the host rock (Fig. 6). Smectite is particularly abundant within the LF. Very few detrital minerals (e.g., quartz, micas) are scattered within the LF, whereas a matrix of mixed organic material and clays is pervasive to the whole specimen.

4.3. Geochemistry

Figs. 7a-d reveal important geochemical features of the LF and their host rock. First, Pb isotope compositions were measured on two different fractions of each of the 14 samples: (1) a clay fraction largely composed of the LF fillings, and (2) a fraction of the host sediment (Table S1). In ^{207}Pb/^{206}Pb-^{204}Pb/^{206}Pb space, all the data points define a linear array with a robust age of 1890 ± 100 Ma (2-sigma error) (Fig. 7a) consistent with literature data (Bonhomme et al., 1982; Bros et al., 1992; Gauthier-Lafaye et al., 1996). The absolute age is key to assessing whether the Pb-Pb age refers to a diachronous Lomagundi or a post-Lomagundi event (see Supple-

mentary material for details). Both the alignment itself and the age of the alignment confirm that if diagenesis had affected these samples, it could only have been *shortly after* sediment deposition of the Francevillian series.

Second, as summarized in Table 1 from the complete data set listed in Supplementary Tables S1-S3 and shown in Figs. 7a-d, the marked geochemical and isotopic contrasts between the LF and their host rock are statistically robust and significant. The LF are characterized by higher Lu/Hf ratios and have higher concentrations of organic C and Zn, but contain less Si, K, Zr, and Hf than their host rock. The Zn contents of the host rock are consistent with the range observed for other black shales worldwide over the last 2.7 Ga (Scott et al., 2013) with the consistency being linked to organic complexes playing an important role in controlling Zn solubility through time (Robbins et al., 2013). The Zn excess (*xs*) in the fillings (*fil*) can be calculated by subtracting a Zn component chemically similar to the host rock (*hr*) from the total concentration. With elemental Fe in organic material being negligible, this gives the simple relationship $[Zn]_{xs} = [Zn]_{fil} - (Zn/Fe)_{hr} \times [Fe]_{fil}$, where brackets refer to concentrations. The average Zn_{xs} values in nine specimens is 111 ± 44 ppm. Consistent Zn excess values are obtained by replacing Fe with other lithogenic elements, such as Y, Zr, Al, or Ti (97–140 ppm).

Zinc is isotopically lighter and Pb more radiogenic in the LF with respect to their host rock. The δ^{66}Zn values of the LF host rock average $0.36 \pm 0.10‰$ (1 sigma) (Table S1), which is well within the lithogenic range (Moynier et al., 2017) but in stark contrast to the average δ^{66}Zn of the LF fillings of $0.10 \pm 0.10‰$, which
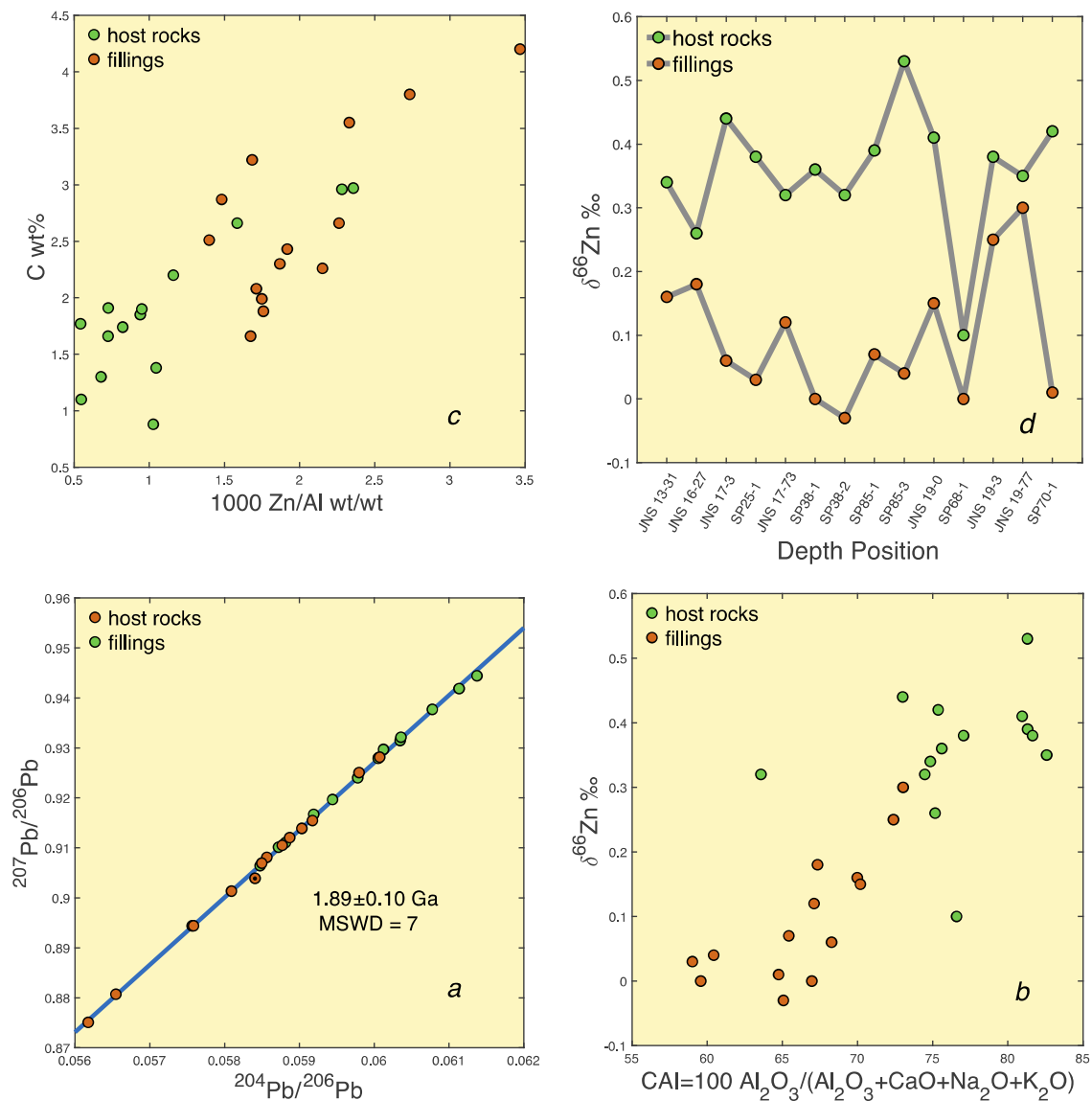
Fig. 7. Geochemistry of the host rock of the LF and their fillings. **(a)** The Pb-Pb linear array (inverse isochron) shows that if the U-Pb chronometer has been reset, it could only have been shortly after sedimentation. The sample with a bull's eye symbol has been left out of the calculations. The error bar includes correction for an MSWD value of 7 and is identical at the same confidence level to the errors calculated by Monte Carlo and bootstrapping. The age is indistinguishable from literature dates (Bonhomme et al., 1982; Bros et al., 1992). **(b)** Relationship between $\delta^{66}Zn$ and the Chemical Index Alteration (CIA) (Nesbitt and Young, 1982). The host rock is dominated by residual material from thoroughly lixiviated soils, whereas the LF fillings contain large fractions of fine-grained material (clays) eroded from the continental surface. **(c)** Correlation between the organic carbon contents of the host rock and the fillings and Zn/Al ratios. The main Zn carrier is clearly associated with the organic component. **(d)** Comparison between the $\delta^{66}Zn$ values of the host rock and the corresponding LF fillings. The $\delta^{66}Zn$ values of the host rock fall within the lithogenic range (0.28 ± 0.13‰ (Moynier et al., 2017)), whereas the fillings are characterized by significantly lower $\delta^{66}Zn$ indicative of organic carbon sediments (Little et al., 2016). Typical error bars are 0.05‰.

a t-test shows to be highly statistically significant ($p = 7 \times 10^{-7}$) (Figs. 7b and d, Table S1).

The $\delta^{13}C$ of a selection of carbon fractions (Table S4) shows no significant difference between the fillings and the host sediments. The average $\delta^{13}C$ value (-34.5 ± 0.5‰) is consistent with Canfield et al.'s (2013) data and falls well within the range of Proterozoic kerogen samples (Des Marais, 1997).

5. Discussion

5.1. Diagenesis

A preliminary issue about the present data set is whether the original geochemistry of the LF and their host rock material has been reset by metamorphism or diagenesis. Iconic Cambrian Lagerstätten, such as the Burgess Shale and Siriuspasset fossil assem-

blages, were buried to temperatures of ∼300 °C, typical of greenschist facies (Butterfield et al., 2007; Gaines et al., 2019; Powell, 2003), which would have been detrimental to the preservation of a primary geochemical signal. By contrast, the Francevillian black shales still contain smectite-rich clays with randomly mixed layers, which attest to a very low diagenetic grade. Persisting smectite relicts within illite at the burial stage limit the temperature of diagenesis to <80 °C (Velde and Vasseur, 1992). This observation is consistent with the maturation of the abundant organic material present in the FB within the oil formation window (<100 °C).

The preservation of an isochronous relationship with the correct geological age indicates that the U-Th-Pb system was not reset by any event potentially taking place after early diagenesis. By extension it can therefore confidently be assumed that neither were Zn isotopes. Over nearly five decades, several authors have pointed
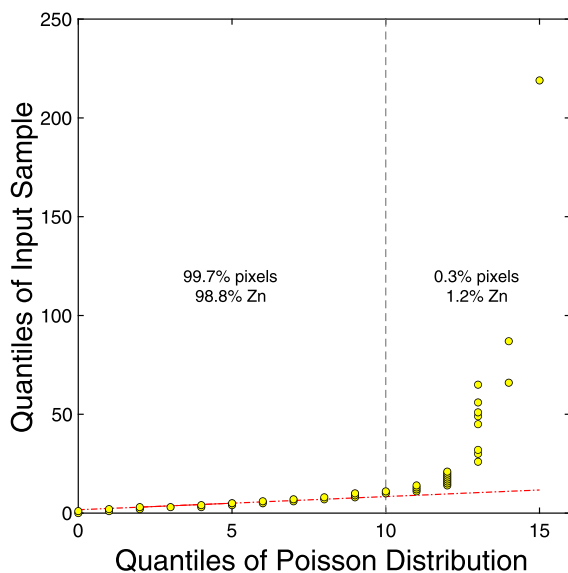
Fig. 8. Quantile-quantile plot comparing, as an example, the observed frequency of the Zn intensity (counts per 10 ms per pixel) measured in the fillings by SR-XRF (shown in Fig. S4) with the frequencies expected from a Poisson (random) distribution. The 1:1 straight-line (in stippled red) shows the perfect correspondence for low-counts pixels, which are the overwhelming majority. The array deviates from linearity at ~10 cps. Only 0.3% of the pixels are outliers (>10 cp 10 ms) with respect to a Poisson distribution and they account for 1.2% of the total Zn concentration of the measured region. The bulk of the Zn inventory, and in particular Zn excesses, therefore should be associated with the carbon-rich background matrix and not with disseminated sulfide crystals. Poisson distributions with similar (Zn outlier)/(total Zn) ratios were found for all the measured regions.

out that Co fluxes to oceanic sediments have remained constant over the last 200 Ma (Dunlea et al., 2015; Krishnaswami, 1976; Zhou and Kyte, 1992). Thibon et al. (2019) demonstrated on cores from the pre-GOE Transvaal Supergroup, South Africa, that Co relative chronometry can be used to estimate sedimentation rates that are within 50% of the rates provided by zircon U-Pb chronology. In order to calculate the time interval Δt during which a series of sediments with thickness Δd (in meters), dry bulk density ρ_{sed} (in g cm^{-3}), and Co concentration [Co] (in ppm) is deposited, they used the mass-conservation relationship:

$$\Delta t = \rho_{sed}[Co]\Delta d / Q_{Co}$$

where Q_{Co} is the modern cobalt deposition rate of 3600 μg cm^{-2} Ma^{-1} (Thibon et al., 2019). With all due caution taken with respect to the uncertainties associated with this approach, this expression suggests that the ~5 m-thick layer of black shales hosting the LF specimens was deposited in about 20,000 years (25 cm ka^{-1}). In the modern ocean, such rapid sedimentation rates are observed along passive margins and in the distal parts of the Bengal and Indus fans (Dutkiewicz et al., 2016)

5.2. The lenticular forms are neither secondary features nor concretions

The LF are not syn-depositional or secondary features formed during burial. Morphology shows that the LF are pre-compaction features that cannot be confused with concretions for two reasons: (1) the brim width is proportional to the size of the specimen, which argues against control by diffusion; and (2) Fig. 4 shows that the silt laminae below the specimen are visibly deflected. The geochemical contrast between the LF and their host rock therefore predates compaction. The persistence of this contrast through diagenesis indicates that only the finest clay material could infiltrate what must have been the LF cavity.

Microtomography shows that the minerals of the brims are the same as those present in the host rock and the interior of the LF (Fig. 4b). The remarkably constant ratio of brim to external diameter of 0.15 ± 0.04 (Fig. 5 inset) over a range of external diameters of 0.2 to 4 cm is consistent with a simple principle of comparative anatomy: for a given species and regardless of the size of individuals, the relative proportions between anatomic units tend to remain similar. If the brims represented diffusion boundary layers, they would be scaled by external physical and chemical parameters, typically in the form of $(Dt)^{1/2}$, with t being the duration of the exchange and temperature-dependent D the diffusion coefficient of the elements moving in and out of the form. The brims would in this case be expected to have the same width in any given layer which is not what is observed.

The distinctly lenticular shape of these objects and the regular progression of their size over time are therefore better reconciled with a biological origin than a sedimentary phenomenon such as minute mud volcanoes or sedimentary nodules.

Finally, should diagenesis from fluid circulation have affected the geochemistry in general, and the Zn isotopes in particular, both the host rock and the LF would have been affected. Post-mortem infiltration of fine-grained sediment into the LF inner cavity should not be mistaken for diagenetic modification. Even in hand specimens, the LF appear as distinct bodies with sharp convex outlines in every dimension, so much so that individual LF are easily freed from their host rock (Fig. 3, Fig. 2 and Fig. S1). As for most bona fide macroscopic fossils, such an effortless release of the LF indicates a strong rheological discontinuity and the lack of a diffusion rim. The fact that Zn and C concentrations and Zn isotopes in the interior of the forms are anomalous with respect to the host rock is evidence that the LF were buried with their geochemical anomaly already in place.

5.3. Pyritization of the circular forms is an uncommon local feature associated with fractures

Sedimentary pyrite is formed by either syngenetic precipitation of minute crystals when at least some layers of the water column are euxinic or during diagenetic sulfate reduction (Canfield et al., 1996; Shen et al., 2002). The scatter of micron-sized pyrite crystals (illustrated by, for example, the Fe and S distribution in Fig. S3) does not support sulfate reduction except along some rare stratigraphic diastems which favor water flow. The bimodal grain size of pyrite crystals strongly argues against pyrite dissolution during diagenetic evolution. Disseminated tiny pyrite crystals (1–3 μm) persist in the matrix next to larger crystals (>30 μm). Because of their high surface energy, small crystals are much more soluble than large crystals. When diagenetic fluids percolate, small crystals dissolve and redeposit onto larger crystals, a mechanism known as Ostwald ripening. Most $\delta^{34}S$ values in both disseminated pyrite (about -25 ± 5‰ (El Albani et al., 2014)) and large crystals (>30 μm) are consistent with the net burial of organic material (Planavsky et al., 2012). Much less frequent $\delta^{34}S$ values > -20‰ may occur at the periphery of large pyrite crystals growing along fractures.

Mass balance also requires that the modal proportion of pyrite in the samples is very small: making the extreme assumption that all S in the sample is in the form of pyrite (i.e., no S in the matrix) and dividing the maximum S concentration in the sample (3000 ppm, Table S3) by the S concentration in pyrite (~36 wt.%), the maximum weight proportion of pyrite is 0.8%. This is in excellent agreement with the ~1% pyrite micro-crystals detected by synchrotron-based scanning X-ray fluorescence microscopy (SR-XRF) imaging (Fig. S3 and Fig. S4). SR-XRF data indicate that the actual Zn concentration in pyrite is in the range of <100 ppm. Scarcity of pyrite has also been pointed out in the Burgess Shale by

Anderson et al. (2021). Even if an extreme value of 2000 ppm Zn in sedimentary pyrite (Large et al., 2014) is adopted, the calculated pyrite abundance would only account for 15 ppm of the rock's Zn inventory, which is insufficient to explain the anomalously light δ^{66}Zn values of the LF fillings (see below). The suggestion (Conway and John, 2014; Little et al., 2016) that diagenetic fluids cause loss of isotopically heavy Zn associated with the formation of modern sedimentary sulfides therefore is not applicable to the Francevillian black shales. Sulfate reduction to pyrite is *not* the process controlling the Zn budget or the Zn isotopic compositions of these samples.

The distinctive Zn anomalies cannot be explained by pyritization either. The large Zn excesses (∼100 ppm) observed in the fillings of the LF are not supported by the rare minute crystals of pyrite observed by SR-XRF (Fig. S3). The distribution maps of S, K, Ca, and Mn do not show any significant co-localization with Zn (see Fig. S5). It can therefore be concluded that Zn is not linked to S, K, Ca, or Mn-containing mineral phases whether in the LF or the host rocks. High-resolution Zn, Fe, and S concentration maps at a micron-scale resolution and ppm-range sensitivity across the specimens distinctly show that the Zn/Fe ratios in pyrite are about two orders of magnitude smaller than the ratios in the matrix. Pyrite crystals are definitely not Zn hot-spots. In addition, the spatial dispersion of Zn throughout the black shales shows that Zn excesses within the LF fillings are randomly distributed across the sample. They follow a Poisson distribution (Fig. 8), and, with rare exceptions, do not follow stratification or fractures.

5.4. The biological nature of the lenticular forms

The singular behavior of Zn, an element particularly abundant in cellular interiors, is correlated with LF organic carbon. Fig. 7c shows how C contents correlate with Zn contents after normalization to Al to account for variable clay abundances. The atomic C/P ratio in the interior of the LF objects is in general high, up to about 140 (average ∼95±27, 1 sigma) and is consistent with the Redfield ratio of modern eukaryotes (Körtzinger et al., 2001). The average δ^{13}C value of −34.5 ± 0.5‰ confirms the lack of major organic carbon oxidation.

With sulfate reduction being dismissed, the most parsimonious explanation for the Zn excesses observed in the fillings of the LF specimens is via an organic carrier. The Zn/Al ratio is up to a factor of 4.3 higher (2.3 on average) in the fillings relative to their host rock and correlates with C content (Fig. 7c). The proportion f_{xs} of organic-bound Zn in the fillings is also remarkably constant at 61 ± 8 wt.%. Such Zn excess values are well within the range of Zn concentrations measured in modern dry phytoplankton (Collier and Edmond, 1984).

δ^{66}Zn values of Archean and Proterozoic pyrite have been shown to be indistinguishable from the lithogenic range (Isson and Planavsky, 2018), which reflects that sulfide minerals do not fractionate Zn isotopes with respect to seawater (Fujii et al., 2014). By contrast, isotopically light Zn isotopes preferentially bind to sulfur-rich amino acid (notably cysteine) (Fujii et al., 2014; Moynier et al., 2017). By subtracting, as above, the host-rock component and taking the mass-balance condition δ^{66}Zn$_{xs}$ = [δ^{66}Zn$_{fil}$ − (1 − f_{xs}) δ^{66}Zn$_{hr}$]/f_{xs} into account, the mean δ^{66}Zn of the organic component of the LF fillings is estimated to be −0.08 ± 0.20‰, a value about 0.4‰ lighter than the value of lithogenic Zn, which for an element as relatively heavy as Zn is a substantial shift. Such a low value is consistent with the range of δ^{66}Zn obtained from phytoplankton cultured in seawater (Köbberich and Vance, 2019; Samanta et al., 2018), and with Archean and Proterozoic kerogen (Isson et al., 2018). The systematically lighter δ^{66}Zn values of the LF fillings with respect to their host rock therefore indicate that

organic material in the LF fillings is not due to infiltration of liquid hydrocarbons but represents primary organic material.

A back-of-the-envelope calculation rooted in the concept of 'minimum Zn quota', which is the lowest amount of zinc per cell that allows for optimal growth (Outten and O'Halloran, 2001), drives home the point that significant phytoplankton biomass was incorporated into the LF. For example, assuming 100 ppm Zn excess in the LF (Table 1), which can be conservatively represented by a 0.1 × 1.0 cm cylinder with a density of 2.5 g cm^{-3}, leads to 3.33 µM Zn. Based on the Zn content of a modern anoxygenic photoautotroph (Konhauser et al., 2018), where one cell has 8.08 × 10^{-18} mol Zn, then 3.33 µM Zn require 4.1 × 10^{11} cells. If the mass of the LF was 77.5 mg (0.031 cm^3 × 2.5 g cm^{-3}), then 5.3 × 10^9 cells were required for each mg of LF. To put this number into context, humans have an estimated 37 trillion cells (Bianconi et al., 2013), which, based on a 70 kg person, is equivalent to 5.3 × 10^8 cells mg^{-1}.

Zinc excesses, high C/P ratios, and low δ^{66}Zn in the LF fillings therefore concur to show that the LF inherited abundant material of organic origin. Infiltration of fine clay mineral into the cavity was probably facilitated by post-mortem bloating of the LF. Zinc is a particularly widespread co-factor of a large number of proteins and a micronutrient of phytoplankton (Moore et al., 2013). Irrespective of whether the LF were prokaryotic or eukaryotic, the present observations validate Zn excesses and Zn isotopes as robust biosignatures consistent with morphological criteria.

The exact kind of life form that the LF represent will be addressed in detail in a separate manuscript, but we will allow ourselves some preliminary speculation here. The internal organic material may consist of cyanobacteria carrion harvested in the nepheloid layer. The presence of a brim therefore suggests that the LF were floating in the water column. This way of living is supported by their settling on different types of substrata. The LF could represent the remnants of prokaryote gigantism, in which case they would be the largest bacteria on record, more than an order of magnitude than the biggest extant species (e.g., up to 750 µm for *Thiomargarita namibiensi*; Schulz and Jørgensen, 2001). It is conceivable that the early appearance gigantism of the LF is in some way related to the nearby Oklo natural nuclear reactors that would have heated the deep interstitial waters and thereby triggered the convection of diagenetic fluids and favored extraction (leaching) of nutrients by interaction of seawater with the host rock.

More fittingly though, the LF could be eukaryotes, which are often suggested to have appeared 300 My later in the early Mesoproterozoic (Knoll et al., 2006). A caveat is that the date of eukaryote emergence is contingent on the reliability of molecular clocks (Butterfield, 2015) and scant field observations. The LF could represent one of the earliest organisms hypothesized by some authors (Javaux and Lepot, 2018; Knoll, 2014), in this case a soft epibenthic eukaryote. A large variety of cm-sized single-cell organisms using sediment grains to build a delicate agglutinated shell exist in the modern abyssal ocean (Gooday et al., 2017). Agglutination of silt material, which appeared multiple times in the evolutionary history of protists (Bowser et al., 2006), would explain the preservation of LF morphological details through fossilization. Given the multiple biological requirements for Zn, its concomitant increase in concentration and LF size up strata may simply reflect the greater Zn demand with increasing cell volume.

6. Conclusions

The geochemical features of ∼2 Ga old objects in Francevillian sediments demonstrate their biogenicity under conditions that may be more typical of deep time on Earth and other planets than the extremely differentiated faunas from the Late Proterozoic and Early Cambrian. We have reached the following conclusions:

a. Diagenetic changes were limited and largely without effect on the mineralogy of the Francevillian LF. Most non-volatile elements, including Pb and Zn and their isotope systematics, were left unchanged.

b. The LF are clearly not concretions or secondary features. The stark geochemical contrasts between the host rock and the LF fillings, notably those associated with Zn, were buried with the LF.

c. Pyritization, when present, is limited to rare fractures and does not affect the bulk of sulfur concentrated in the organic material and leaves the Zn budget largely unaffected.

d. The criteria used in this work are heavily biased towards geochemical observations and demonstrate the biogenic nature of the lenticular forms. These organisms probably represent clay-clad protists of exceptionally large size.

e. The decision tree leading to infer the biogenicity of the Francevillian LF may be extended in deep time to other sedimentary features, while the approach itself of investigating biogenicity of fossilized remnants using Zn isotopes together with other isotopes (e.g., S and C) and organic tracers, may be extended to extraterrestrial samples.

CRediT authorship contribution statement

A.E.A. designed the research. A.E.A., F.A., J.B.T., A.S., E.C.F. and K.O.K. wrote the manuscript. A.E.A., E.C.F., and J.N.G. did the field work. J.N.G., C.F., J.N.G., and A.E.A. prepared the samples and performed XRD analyses and models. A.M. performed X-Ray microtomography. A.E.A. analyzed morphology, A.R. analyzed carbon and sulfur concentrations. A.C.P.W. analyzed carbon isotopes. A.L. analyzed Zn and Pb isotope compositions with assistance from J.B.T. A.S. carried out the synchrotron experiments and processed the data.

Declaration of competing interest

The authors declare that they have no known competing financial interests or personal relationships that could have appeared to influence the work reported in this paper.

Data availability

Data will be made available on request.

Acknowledgements

Appendix A. Supplementary material

Supplementary material related to this article can be found online at https://doi.org/10.1016/j.epsl.2023.118169.

References

Albarède, F., Telouk, P., Blichert-Toft, J., Boyet, M., Agranier, A., Nelson, B., 2004. Precise and accurate isotopic measurements using multiple-collector ICPMS. Geochim. Cosmochim. Acta 68, 2725–2744.

Allwood, A.C., Rosing, M.T., Flannery, D.T., Hurowitz, J.A., Heirwegh, C.M., 2018. Reassessing evidence of life in 3,700-million-year-old rocks of Greenland. Nature 563, 241–244.

Anderson, R.P., Tosca, N.J., Saupe, E.E., Wade, J., Briggs, D.E., 2021. Early formation and taphonomic significance of kaolinite associated with Burgess Shale fossils. Geology 49, 355–359.

Beyssac, O., Brunet, F., Petitet, J.-P., Goffé, B., Rouzaud, J.-N., 2003. Experimental study of the microtextural and structural transformations of carbonaceous materials under pressure and temperature. Eur. J. Mineral. 15, 937–951.

Beyssac, O., Goffé, B., Chopin, C., Rouzaud, J., 2002. Raman spectra of carbonaceous material in metasediments: a new geothermometer. J. Metamorph. Geol. 20, 859–871.

Bianconi, E., Piovesan, A., Facchin, F., Beraudi, A., Casadei, R., Frabetti, F., Vitale, L., Pelleri, M.C., Tassani, S., Piva, F., 2013. An estimation of the number of cells in the human body. Ann. Hum. Biol. 40, 463–471.

Bonhomme, M., Gauthier-Lafaye, F., Weber, F., 1982. An example of lower proterozoic sediments: the Francevillian in Gabon. Precambrian Res. 18, 87–102.

Bowser, S.S., Habura, A., Pawlowski, J., Katz, L., Bhattacharya, D., 2006. Molecular evolution of Foraminifera. In: Genomics and Evolution of Microbial Eukaryotes, pp. 78–93.

Bros, R., Stille, P., Gauthier-Lafaye, F., Weber, F., Clauer, N., 1992. Sm-Nd isotopic dating of proterozoic clay material: an example from the Francevillian sedimentary series, Gabon. Earth Planet. Sci. Lett. 113, 207–218.

Butterfield, N.J., 2007. Macroevolution and macroecology through deep time. Palaeontol. 50, 41–55.

Butterfield, N.J., 2015. Early evolution of the Eukaryota. Palaeontol. 58, 5–17.

Butterfield, N.J., Balthasar, U., Wilson, L.A., 2007. Fossil diagenesis in the Burgess Shale. Palaeontol. 50, 537–543.

Canfield, D.E., Lyons, T.W., Raiswell, R., 1996. A model for iron deposition to euxinic Black Sea sediments. Am. J. Sci. 296, 818–834.

Canfield, D.E., Ngombi-Pemba, L., Hammarlund, E.U., Bengtson, S., Chaussidon, M., Gauthier-Lafaye, F., Meunier, A., Riboulleau, A., Rollion-Bard, C., Rouxel, O., 2013. Oxygen dynamics in the aftermath of the great oxidation of Earth's atmosphere. Proc. Natl. Acad. Sci. 110, 16736–16741.

Carignan, J., Hild, P., Mevelle, G., Morel, J., Yeghicheyan, D., 2001. Routine analyses of trace elements in geological samples using flow injection and low pressure on-line liquid chromatography coupled to ICP-MS: a study of geochemical reference materials BR, DR-N, UB-N, AN-G and GH. Geostand. Newsl. 25, 187–198.

Collier, R.W., Edmond, J.M., 1984. The trace element geochemistry of marine biogenic particulate matter. Prog. Oceanogr. 13, 113–199.

Conway, T.M., John, S.G., 2014. The biogeochemical cycling of zinc and zinc isotopes in the North Atlantic Ocean. Glob. Biogeochem. Cycles 28, 1111–1128.

Des Marais, D.J., 1997. Isotopic evolution of the biogeochemical carbon cycle during the Proterozoic Eon. Org. Geochem. 27, 185–193.

Dunlea, A.G., Murray, R.W., Sauvage, J., Pockalny, R.A., Spivack, A.J., Harris, R.N., D'Hondt, S., 2015. Cobalt-based age models of pelagic clay in the South Pacific Gyre. Geochem. Geophys. Geosyst. 16, 2694–2710.

Dutkiewicz, A., Müller, R.D., Hogg, A.M., Spence, P., 2016. Vigorous deep-sea currents cause global anomaly in sediment accumulation in the Southern Ocean. Geology 44, 663–666.

Eisele, J., Abouchami, W., Galer, S.J.G., Hofmann, A.W., 2003. The 320 kyr Pb isotope evolution of Mauna Kea lavas recorded in the HSDP-2 drill core. Geochem. Geophys. Geosyst. 4. https://doi.org/10.1029/2002GC000339.

El Albani, A., Bengtson, S., Canfield, D.E., Bekker, A., Macchiarelli, R., Mazurier, A., Hammarlund, E.U., Boulvais, P., Dupuy, J.-J., Fontaine, C., 2010. Large colonial organisms with coordinated growth in oxygenated environments 2.1 Gyr ago. Nature 466, 100–104.

El Albani, A., Bengtson, S., Canfield, D.E., Riboulleau, A., Rollion Bard, C., Macchiarelli, R., Ngombi Pemba, L., Hammarlund, E., Meunier, A., Moubiya Mouele, I., 2014. The 2.1 Ga old Francevillian biota: biogenicity, taphonomy and biodiversity. PLoS ONE 9, e99438.

El Albani, A., Mangano, M.G., Buatois, L.A., Bengtson, S., Riboulleau, A., Bekker, A., Konhauser, K., Lyons, T., Rollion-Bard, C., Bankole, O., 2019. Organism motility

in an oxygenated shallow-marine environment 2.1 billion years ago. Proc. Natl. Acad. Sci. 116, 3431–3436.

Fujii, T., Moynier, F., Blichert-Toft, J., Albarede, A.F., 2014. Density functional theory estimation of isotope fractionation of Fe, Ni, Cu, and Zn among species relevant to geochemical and biological environments. Geochim. Cosmochim. Acta 140, 553–576.

Gaines, R.R., Lombardo, A.J., Holzer, I.O., Caron, J.-B., 2019. The limits of burgess shale-type preservation: assessing the evidence for preservation of the blood protein hemocyanin in the burgess shale. Palaios 34, 291–299.

Gangidine, A., Walter, M.R., Havig, J.R., Jones, C., Sturmer, D.M., Czaja, A.D., 2021. Trace element concentrations associated with mid-Paleozoic microfossils as biosignatures to aid in the search for life. Life 11, 142.

Gauthier-Lafaye, F., 1986. Les gisements d'uranium du Gabon et les reacteurs d'Oklo. Modèle métallogénique de gîtes à fortes teneurs du protérozoique inférieur. Sci. Géol. Bull. Mém. Strasbourg 78.

Gauthier-Lafaye, F., Bros, R., Stille, P., 1996. Pb isotope pe systematics on diagenetic clays: an example from proterozoic black shales of the franceville basin (Gabon). Chem. Geol. 133, 243–250.

Gauthier-Lafaye, F., Weber, F., Ohmoto, H., 1989. Natural fission reactors of Oklo. Econ. Geol. 84, 2286–2295.

Gooday, A.J., Holzmann, M., Caulle, C., Goineau, A., Kamenskaya, O., Weber, A.A.-T., Pawlowski, J., 2017. Giant protists (xenophyophores, Foraminifera) are exceptionally diverse in parts of the abyssal eastern Pacific licensed for polymetallic nodule exploration. Biol. Conserv. 207, 106–116.

Hickman-Lewis, K., Cavalazzi, B., Sorieul, S., Gautret, P., Foucher, F., Whitehouse, M.J., Jeon, H., Georgelin, T., Cockell, C.S., Westall, F., 2020. Metallomics in deep time and the influence of ocean chemistry on the metabolic landscapes of Earth's earliest ecosystems. Sci. Rep. 10, 1–16.

Hickman-Lewis, K., Garwood, R.J., Brasier, M.D., Goral, T., Jiang, H., McLoughlin, N., Wacey, D., 2016. Carbonaceous microstructures from sedimentary laminated chert within the 3.46 Ga Apex Basalt, Chinaman Creek locality, Pilbara, Western Australia. Precambrian Res. 278, 161–178.

Isson, T.T., Love, G.D., Dupont, C.L., Reinhard, C.T., Zumberge, A.J., Asael, D., Gueguen, B., McCrow, J., Gill, B.C., Owens, J., 2018. Tracking the rise of eukaryotes to ecological dominance with zinc isotopes. Geobiology 16, 341–352.

Isson, T.T., Planavsky, N.J., 2018. Reverse weathering as a long-term stabilizer of marine pH and planetary climate. Nature 560, 471–475.

Javaux, E.J., Lepot, K., 2018. The Paleoproterozoic fossil record: implications for the evolution of the biosphere during Earth's middle-age. Earth-Sci. Rev. 176, 68–86.

Knoll, A.H., 2014. Paleobiological perspectives on early eukaryotic evolution. Cold Spring Harb. Perspect. Biol. 6, a016121.

Knoll, A.H., Javaux, E.J., Hewitt, D., Cohen, P., 2006. Eukaryotic organisms in Proterozoic oceans. Philos. Trans. R. Soc. Lond. B, Biol. Sci. 361, 1023–1038.

Köbberich, M., Vance, D., 2019. Zn isotope fractionation during uptake into marine phytoplankton: implications for oceanic zinc isotopes. Chem. Geol. 523, 154–161.

Konhauser, K.O., Robbins, L.J., Alessi, D.S., Flynn, S.L., Gingras, M.K., Martinez, R.E., Kappler, A., Swanner, E.D., Li, Y.-L., Crowe, S.A., 2018. Phytoplankton contributions to the trace-element composition of Precambrian banded iron formations. Bulletin 130, 941–951.

Körtzinger, A., Hedges, J.I., Quay, P.D., 2001. Redfield ratios revisited: removing the biasing effect of anthropogenic CO2. Limnol. Oceanogr. 46, 964–970.

Kouketsu, Y., Mizukami, T., Mori, H., Endo, S., Aoya, M., Hara, H., Nakamura, D., Wallis, S., 2014. A new approach to develop the R aman carbonaceous material geothermometer for low-grade metamorphism using peak width. Isl. Arc 23, 33–50.

Krishnaswami, S., 1976. Authigenic transition elements in Pacific pelagic clays. Geochim. Cosmochim. Acta 40, 425–434.

Large, R.R., Halpin, J.A., Danyushevsky, L.V., Maslennikov, V.V., Bull, S.W., Long, J.A., Gregory, D.D., Lounejeva, E., Lyons, T.W., Sack, P.J., 2014. Trace element content of sedimentary pyrite as a new proxy for deep-time ocean–atmosphere evolution. Earth Planet. Sci. Lett. 389, 209–220.

Little, S.H., Vance, D., McManus, J., Severmann, S., 2016. Key role of continental margin sediments in the oceanic mass balance of Zn and Zn isotopes. Geology 44, 207–210.

Mänd, K., Lalonde, S.V., Robbins, L.J., Thoby, M., Paiste, K., Kreitsmann, T., Paiste, P., Reinhard, C.T., Romashkin, A.E., Planavsky, N.J., Kirsimae, K., Lepland, A., Konhauser, K.O., 2020. Palaeoproterozoic oxygenated oceans following the Lomagundi-Jatuli Event. Nat. Geosci. 13, 302–306.

Marshall, C.P., Javaux, E.J., Knoll, A.H., Walter, M.R., 2005. Combined micro-Fourier transform infrared (FTIR) spectroscopy and micro-Raman spectroscopy of Proterozoic acritarchs: a new approach to palaeobiology. Precambrian Res. 138, 208–224.

Martin, A.P., Condon, D., Prave, A.R., Melezhik, V.A., Lepland, A., Fallick, A.E., 2013. Dating the termination of the Palaeoproterozoic Lomagundi-Jatuli carbon isotopic event in the North Transfennoscandian Greenstone Belt. Precambrian Res. 224, 160–168.

Martin, A.P., Prave, A., Condon, D., Lepland, A., Fallick, A.E., Romashkin, A., Medvedev, P., Rychanchik, D., 2015. Multiple Palaeoproterozoic carbon burial episodes and excursions. Earth Planet. Sci. Lett. 424, 226–236.

Melezhik, V.A., Fallick, A.E., Martin, A.P., Condon, D.J., Kump, L.R., Brasier, A.T., 2013. The greatest perturbation of the global carbon cycle: the Lomagundi-Jatuli isotopic event. In: Melezhik, V., Prave, A.R., Hanski, E.J., Fallick, A.E., Lepland, A., Kump, L.R., Strauss, H. (Eds.), Reading the Archive of Earth's Oxygenation. In: Frontiers in Earth Sciences. Springer, Heidelberg, pp. 1111–1150.

Mercuzot, M., Thomazo, C., Schnyder, J., Pellenard, P., Baudin, F., Pierson-Wickmann, A.-C., Sans-Jofre, P., Bourquin, S., Beccaletto, L., Santoni, A.-L., 2021. Carbon and nitrogen cycle dynamic in continental Late-Carboniferous to Early Permian Basins of Eastern Pangea (Northeastern Massif Central, France). Front. Earth Sci. 615.

Moore, C., Mills, M., Arrigo, K., Berman-Frank, I., Bopp, L., Boyd, P., Galbraith, E., Geider, R., Guieu, C., Jaccard, S., 2013. Processes and patterns of oceanic nutrient limitation. Nat. Geosci. 6, 701–710.

Mossman, D.J., 2001. Hydrocarbon habitat of the paleoproterozoic franceville series, republic of Gabon. Energy Sources 23, 45–53.

Mossman, D.J., Gauthier-Lafaye, F., Jackson, S.E., 2005. Black shales, organic matter, ore genesis and hydrocarbon generation in the Paleoproterozoic Franceville Series, Gabon. Precambrian Res. 137, 253–272.

Moynier, F., Vance, D., Fujii, T., Savage, P., 2017. The isotope geochemistry of zinc and copper. Rev. Mineral. Geochem. 82, 543–600.

Nesbitt, H.W., Young, G.M., 1982. Early Proterozoic climates and plate motions inferred from major element chemistry of lutites. Nature 299, 715–717.

Neveu, M., Hays, L.E., Voytek, M.A., New, M.H., Schulte, M.D., 2018. The ladder of life detection. Astrobiology 18, 1375–1402.

Olcott Marshall, A., Marshall, C.P., 2015. Vibrational spectroscopy of fossils. Palaeontol. 58, 201–211.

Outten, C.E., O'Halloran, T.V., 2001. Femtomolar sensitivity of metalloregulatory proteins controlling zinc homeostasis. Science 292, 2488–2492.

Pichat, S., Douchet, C., Albarède, F., 2003. Zinc isotope variations in deep-sea carbonates from the eastern equatorial Pacific over the last 175 ka. Earth Planet. Sci. Lett. 210, 167–178.

Planavsky, N.J., Bekker, A., Hofmann, A., Owens, J.D., Lyons, T.W., 2012. Sulfur record of rising and falling marine oxygen and sulfate levels during the Lomagundi event. Proc. Natl. Acad. Sci. 109, 18300–18305.

Porter, S.J., Selby, D., Cameron, V., 2014. Characterising the nickel isotopic composition of organic-rich marine sediments. Chem. Geol. 387, 12–21.

Powell, W., 2003. Greenschist-facies metamorphism of the Burgess Shale and its implications for models of fossil formation and preservation. Can. J. Earth Sci. 40, 13–25.

Quirico, E., Montagnac, G., Rouzaud, J.-N., Bonal, L., Bourot-Denise, M., Duber, S., Reynard, B., 2009. Precursor and metamorphic condition effects on Raman spectra of poorly ordered carbonaceous matter in chondrites and coals. Earth Planet. Sci. Lett. 287, 185–193.

Reynaud, J.-Y., Trentesaux, A., El Albani, A., Aubineau, J., Ngombi-Pemba, L., Guiyeligou, G., Bouton, P., Gauthier-Lafaye, F., Weber, F., 2018. Depositional setting of the 2·1 Ga Francevillian macrobiota (Gabon): rapid mud settling in a shallow basin swept by high-density sand flows. Sedimentology 65, 670–701.

Robbins, L., Lalonde, S., Saito, M.A., Planavsky, N., Mloszewska, A., Pecoits, E., Scott, C., Dupont, C., Kappler, A., Konhauser, K., 2013. Authigenic iron oxide proxies for marine zinc over geological time and implications for eukaryotic metallome evolution. Geobiology 11, 295–306.

Rosing, M.T., 1999. 13C-depleted carbon microparticles in >3700-Ma sea-floor sedimentary rocks from West Greenland. Science 283, 674–676.

Samanta, M., Ellwood, M.J., Strzepek, R.F., 2018. Zinc isotope fractionation by Emiliania huxleyi cultured across a range of free zinc ion concentrations. Limnol. Oceanogr. 63, 660–671.

Schulz, H.N., Jørgensen, B.B., 2001. Big bacteria. Annu. Rev. Microbiol. 55, 105–137.

Scott, C., Planavsky, N.J., Dupont, C.L., Kendall, B., Gill, B.C., Robbins, L.J., Husband, K.F., Arnold, G.L., Wing, B.A., Poulton, S.W., 2013. Bioavailability of zinc in marine systems through time. Nat. Geosci. 6, 125–128.

Sforna, M.-C., Van Zuilen, M., Philippot, P., 2014. Structural characterization by Raman hyperspectral mapping of organic carbon in the 3.46 billion-year-old Apex chert, Western Australia. Geochim. Cosmochim. Acta 124, 18–33.

Sforna, M.C., Loron, C.C., Demoulin, C.F., François, C., Cornet, Y., Lara, Y.J., Grolimund, D., Ferreira Sanchez, D., Medjoubi, K., Somogyi, A., 2022. Intracellular bound chlorophyll residues identify 1 Gyr-old fossils as eukaryotic algae. Nat. Commun. 13, 1–8.

Shen, Y., Canfield, D.E., Knoll, A.H., 2002. Middle Proterozoic ocean chemistry: evidence from the McArthur Basin, northern Australia. Am. J. Sci. 302, 81–109.

Solé, V.A., Papillon, E., Cotte, M., Walter, P., Susini, J., 2007. A multiplatform code for the analysis of energy-dispersive X-ray fluorescence spectra. Spectrochim. Acta, Part B, At. Spectrosc. 62, 63–68.

Somogyi, A., Medjoubi, K., Baranton, G., Le Roux, V., Ribbens, M., Polack, F., Philippot, P., Samama, J.-P., 2015. Optical design and multi-length-scale scanning spectro-microscopy possibilities at the Nanoscopium beamline of Synchrotron Soleil. J. Synchrotron Radiat. 22, 1118–1129.

Tashiro, T., Ishida, A., Hori, M., Igisu, M., Koike, M., Méjean, P., Takahata, N., Sano, Y., Komiya, T., 2017. Early trace of life from 3.95 Ga sedimentary rocks in Labrador, Canada. Nature 549, 516–518.

Thibon, F., Blichert-Toft, J., Tsikos, H., Foden, J., Albalat, E., Albarede, F., 2019. Dynamics of oceanic iron prior to the Great Oxygenation Event. Earth Planet. Sci. Lett. 506, 360–370.

Tufail, A., Li, H., Naeem, A., Li, T., 2018. Leaf cell membrane stability-based mechanisms of zinc nutrition in mitigating salinity stress in rice. Plant Biol. 20, 338–345.

Twining, B.S., Baines, S.B., 2013. The trace metal composition of marine phytoplankton. Annu. Rev. Mar. Sci. 5, 191–215.

Velde, B., Vasseur, G., 1992. Estimation of the diagenetic smectite to illite transformation in time-temperature space. Am. Mineral. 77, 967–976.

Wacey, D., 2009. Early Life on Earth: a Practical Guide. Springer Science & Business Media.

Weber, F., 1968. Une série précambrienne du Gabon: le Francevillien. Sédimentologie, géochimie, relations avec les gites minéraux associés. Sci. Géol. Bull. Mém. Strasbourg 28.

Weber, T., John, S., Tagliabue, A., DeVries, T., 2018. Biological uptake and reversible scavenging of zinc in the global ocean. Science 361, 72–76.

Zhou, L., Kyte, F.T., 1992. Sedimentation history of the South Pacific pelagic clay province over the last 85 million years inferred from the geochemistry of Deep Sea Drilling Project Hole 596. Paleoceanography 7, 441–465.